


Article

# Synthesis of Side-Chain Liquid Crystalline Polyacrylates with Bridged Stilbene Mesogens

Gen-ichi Konishi <sup>1,2,\*</sup>, Yuki Sawatari <sup>1</sup>, Riki Iwai <sup>1</sup>, Takuya Tanaka <sup>1</sup>, Yoshimichi Shimomura <sup>1</sup> and Masatoshi Tokita <sup>1,2</sup> <sup>1</sup> Department of Chemical Science and Engineering, Institute of Science Tokyo, Tokyo 152-8552, Japan<sup>2</sup> Department of Polymer Chemistry, Tokyo Institute of Technology, Tokyo 152-8552, Japan

\* Correspondence: konishi.g.579e@m.isct.ac.jp or konishi.g.aa@m.titech.ac.jp

**Abstract:** In recent years,  $\pi$ -conjugated liquid crystalline molecules with optoelectronic functionalities have garnered considerable attention, and integrating these molecules into side-chain liquid crystalline polymers (SCLCPs) holds potential for developing devices that are operational near room temperature. However, it is difficult to design SCLCPs with excellent processability because liquid crystalline mesogens are rigid rods, have low solubility in organic solvents, and have a high isotropization temperature. Recently, we developed near-room-temperature  $\pi$ -conjugated nematic liquid crystals based on “bridged stilbene”. In this work, we synthesized a polyacrylate SCLCP incorporating a bridged stilbene that exhibited a nematic phase near room temperature and could maintain liquid crystallinity for more than three months. We conducted a thorough phase structure analysis and evaluated the optical properties. The birefringence values of the resulting polymers were higher than those of the corresponding monomers because of the enhanced order parameters due to the polymer effect. In addition, the synthesized polymers inherited mesogen-derived AIE properties, with high quantum yields ( $\Phi_f = 0.14$ – $0.35$ ) in the solid state. It is noteworthy that the maximum fluorescence wavelength exhibited a redshift of greater than 27 nm as a consequence of film formation. Thus, several unique characteristics of the SCLCPs are unattainable with small molecular systems.



**Citation:** Konishi, G.-i.; Sawatari, Y.; Iwai, R.; Tanaka, T.; Shimomura, Y.; Tokita, M. Synthesis of Side-Chain Liquid Crystalline Polyacrylates with Bridged Stilbene Mesogens. *Molecules* **2024**, *29*, 5220. <https://doi.org/10.3390/molecules29215220>

Academic Editors: Ana Catarina Trindade, João Canejo and Pedro Marques De Almeida

Received: 30 September 2024

Revised: 31 October 2024

Accepted: 3 November 2024

Published: 4 November 2024



**Copyright:** © 2024 by the authors. Licensee MDPI, Basel, Switzerland. This article is an open access article distributed under the terms and conditions of the Creative Commons Attribution (CC BY) license (<https://creativecommons.org/licenses/by/4.0/>).

**Keywords:** side-chain liquid crystalline polymer; nematic liquid crystal; polyacrylate;  $\pi$ -conjugated mesogen; birefringence; aggregation-induced emission

## 1. Introduction

Liquid crystal polymers are widely used in industrial applications due to their excellent processability and favorable material properties [1–14]. Of particular interest are side-chain liquid crystal polymers (SCLCPs) [15–25], in which mesogenic units are attached to the side chains of linear polymers such as polyacrylate and polymethacrylate. SCLCPs exhibit liquid crystalline phases over a broader temperature range than small molecule liquid crystals and mimic the behavior of small molecule liquid crystals above the glass transition temperature ( $T_g$ ). This liquid crystalline nature allows for the molecular orientation to be controlled by external fields such as mechanical stress, electric fields, and magnetic fields [1–14]. In addition, the molecular orientation of LC polymers can be controlled using anisotropic surfaces (as in this study) and photoalignment (e.g., [16]). Additionally, SCLCPs can form nanostructures through higher order smectic and columnar phases [26–29]. Below  $T_g$ , the liquid crystal phase that exists above  $T_g$  can be vitrified, retaining its anisotropic properties. Among liquid crystal phases, the nematic (N) phase is the most fluid, is highly responsive to external fields, and is suitable for large-area applications [30]. These properties, unique to the N phase, distinguish it from other liquid crystal phases and extend its range of applications beyond traditional uses, including displays [31,32] and polarizing films, into advanced optical materials. The properties exhibited by SCLCPs are highly attractive for the development of materials that leverage the unique optical, luminescent,

and electronic properties of  $\pi$ -conjugated systems [33–46]. In particular, SCLCPs with liquid crystalline organic semiconductors in the side chains can be one of the most powerful tools for fabricating film-like devices with bulk arrays of organic semiconductors. In other words, it is effective for the realization of advanced materials based on functional liquid crystalline  $\pi$ -conjugated molecules, such as displays and molecular electronics. However,  $\pi$ -conjugated molecules with functional groups typically have high melting points, and SCLCPs incorporating these as mesogens often struggle to exhibit the nematic (N) phase or only exhibit it at elevated temperatures above 100 °C [45]. In addition, the introduction of a long-chain alkyl group into the mesogen lowers the isotropization temperature but tends to produce a smectic phase with high crystallinity and low operability [47]. As a result, it is challenging to achieve room temperature N-phase behavior in SCLCPs that feature  $\pi$ -conjugated mesogens with photo/electronic functionality.

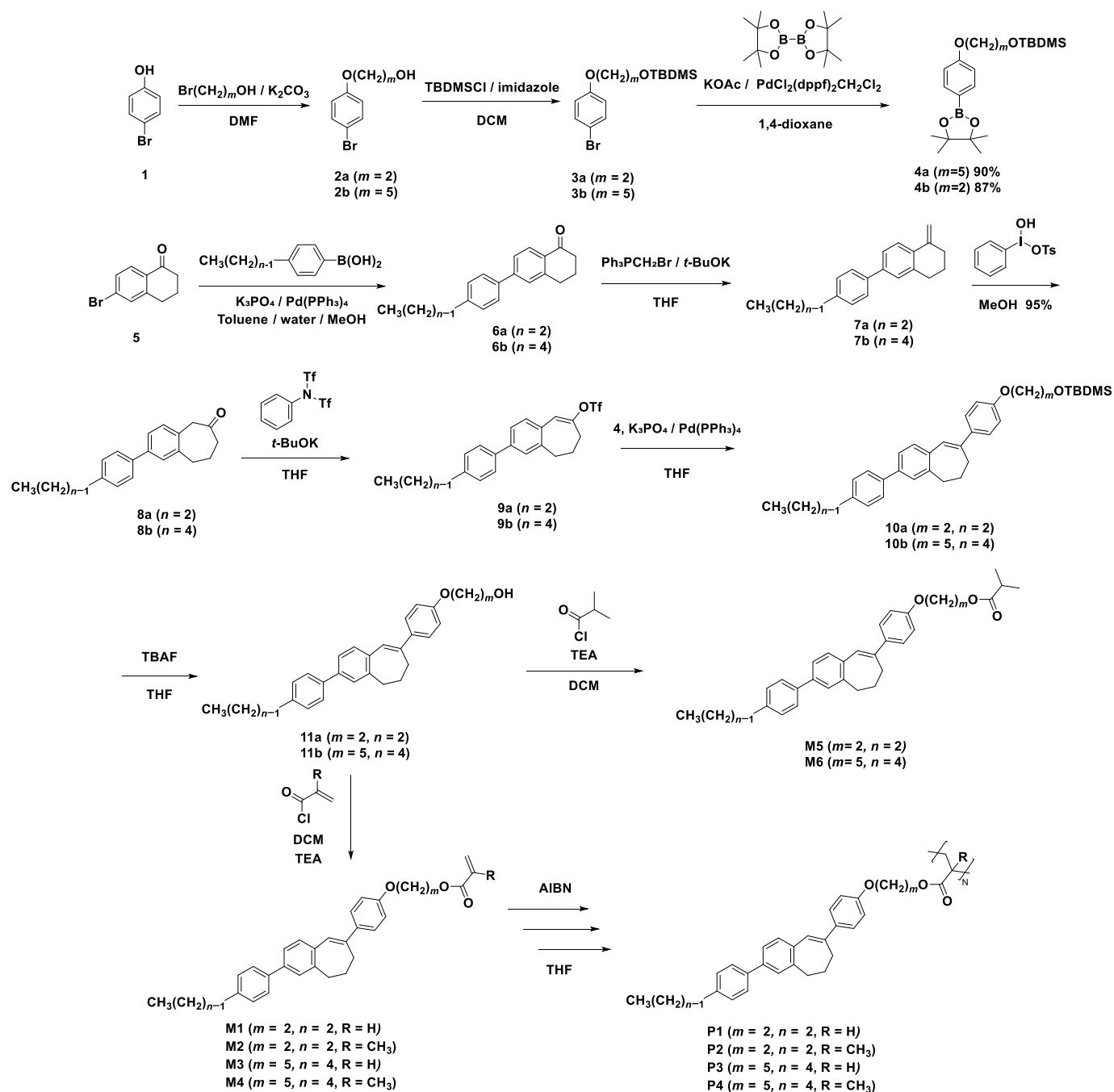
Recently, we developed a novel aggregation-induced emission luminogen (AIEgen) [48–54], “seven-membered bridged stilbene”, based on 4-phenyl stilbene (PST) with a seven-membered ring structure, specifically 3,8-diphenyl-6,7-dihydro-5H-benzo[7]annulene (DPB[7]) [55–57]. We reported that DPB[7], when modified with appropriate alkyl tails at both ends, exhibits the N phase around room temperature [58]. This bridged stilbene liquid crystal (LC) possesses the unique ability to maintain the N phase over a wide temperature range while exhibiting luminescent properties. Such  $\pi$ -conjugated liquid crystals with low isotropization temperatures have the potential to overcome various limitations of conventional SCLCPs. Using this LC, we have designed a  $\pi$ -conjugated SCLCP that exhibits the N phase at room temperature.

In this study, we synthesized polyacrylate and polymethacrylate SCLCP with the DPB[7] mesogen, which exhibits a nematic phase at room temperature. We analyzed the detailed phase structure and evaluated the birefringence and photophysical properties. Our findings revealed several unique properties of SCLCPs that are not achievable with small molecule systems.

## 2. Results and Discussion

### 2.1. Synthesis of Monomers and Polymers

We synthesized side-chain liquid crystalline polyacrylates and polymethacrylates incorporating the 3,8-diphenyl-6,7-dihydro-5H-benzo[7]annulene (DPB[7]) skeleton with alkyl terminals (carbon number:  $n = 2, 4$ ), alkoxy spacers (carbon number:  $m = 2, 5$ ), and various terminal ester groups. The chemical structures and synthetic procedures of the monomers (M1–M4), polymers (P1–P4), and model compounds (M5 and M6) are illustrated in Scheme 1. The synthesis of the monomers can be outlined as follows: Suzuki–Miyaura cross-coupling reaction [59,60] between 6-bromo-1-tetralone (5) and 4-alkylphenylboronic acid (with alkyl group carbon numbers:  $m = 2, 4$ ) provided 6, followed by a Wittig reaction to yield 7; a ring expansion reaction using hypervalent iodine reagent [hydroxy(tosyloxy)iodo]benzene (HTIB) then produced 8; triflation of the carbonyl group yielded 9, and subsequent Suzuki–Miyaura cross-coupling of 9 with 4-alkoxyphenylboronic acid pinacol esters (alkoxy group carbon numbers:  $n = 2, 5$ ) provided 10; deprotection of the *tert*-butyldimethylsilyl (TBDMS) group of 10 using tetrabutylammonium fluoride (TBAF) resulted in 11. Finally, the introduction of various acyl chlorides afforded the acrylic monomers (M1 and M3), methacrylic monomers (M2 and M4), and isobutyrate derivatives (M5 and M6). The monomers were purified via column chromatography on silica gel and recrystallization. The chemical structures of the monomers and model compounds were confirmed through  $^1\text{H-NMR}$ ,  $^{13}\text{C-NMR}$ , FT-IR, and high-resolution mass spectrometry (HRMS). These spectral data and the synthesis of 1–4 are provided in Supporting Information (SI).



**Scheme 1.** Synthesis of acrylic monomers (**M1** and **M3**), methacrylic monomers (**M2** and **M4**), and model compounds of monomer (**M5** and **M6**) with **DPB[7]** skeleton and flexible chains ( $m + 1, n$ ), and corresponding polymers (**P1–P4**).

Radical polymerization of the acrylic monomers (**M1** and **M3**) and methacrylic monomers (**M2** and **M4**) was conducted using 6.5 wt% azobisisobutyronitrile (AIBN) as the initiator, resulting in the corresponding polymers (**P1–P4**). The crude polymers were purified by reprecipitation in methanol. The polymer structures were confirmed by  $^1\text{H-NMR}$  and  $^{13}\text{C-NMR}$  spectroscopy. The number-average molecular weight ( $M_n$ ) and weight-average molecular weight ( $M_w$ ) of the polymers were determined via gel permeation chromatography using polystyrene standards. Furthermore, thermogravimetric analysis (TGA) measurements were performed on **P1–P4** at a rate of  $20\text{ }^\circ\text{C min}^{-1}$  (Figures S1–S4), determining degradation temperatures at a 10% weight loss ( $T_{10}$ ). The results are summa-

rized in Table 1. The polymethacrylates exhibited higher molecular weights compared with the polyacrylates.

**Table 1.** The results of polymerization: yields,  $M_n$ ,  $M_w$ , polydispersity indexes ( $M_w/M_n$ ), and degradation temperature at 10% weight loss ( $T_{10}$ ) of **P1–P4**.

| Entry     | Yield (%) | $M_n$  | $M_w$  | $M_w/M_n$ | $T_{10}$ [°C] |
|-----------|-----------|--------|--------|-----------|---------------|
| <b>P1</b> | 40        | 3000   | 5200   | 1.70      | 410           |
| <b>P2</b> | 34        | 10,400 | 20,000 | 1.93      | 409           |
| <b>P3</b> | 19        | 5000   | 7000   | 1.40      | 413           |
| <b>P4</b> | 10        | 17,100 | 26,500 | 1.55      | 412           |

## 2.2. Phase Transition Behaviors

Liquid crystalline phases of the polymers, monomers, and model compounds were identified using polarized optical microscopy (POM). Phase transition temperatures and enthalpies were determined through differential scanning calorimetry (DSC). POM observations suggested that **M1** and **M2** exhibited only the nematic (N) phase, while **M3** and **M4** exhibited both the N phase and the smectic A (SmA) phase. It is suspected that the vinyl groups in **M1–M4** underwent either conversion to another compound or oligomerization owing to thermal reactions. Therefore, we synthesized model compounds (**M5** and **M6**) in which the (meth)acrylate group was replaced with an isobutyrate group. **M5** and **M6** were used for comparison with the monomers and polymers in subsequent analyses. The phase transition temperatures and enthalpies ( $\Delta H$ ) of **M5** and **M6** and **P1–P4** are summarized in Table 2, and the typical POM images of **P2** and **P4** are illustrated in Figure 1. The DSC curves for **M5** (second scan), **M6** (second scan), and **P1–P4** (third scan) are shown in Figures S5–S10, while the POM images for **M5**, **M6**, **P1**, **P3**, and the rest of **P2** and **P4** are shown in Figures S11–S16.

**Table 2.** Phase transition temperature [°C] (enthalpy  $\Delta H$  [kJ mol<sup>-1</sup>]) and the range of LC phase ( $\Delta T_{LC}$  [°C]) of **DPB[7]** monomers (**M5** and **M6**) and **DPB[7]** polymers (**P1–P4**) upon heating and cooling at a rate of 10 °C min<sup>-1</sup> (Cr and Cr2: crystal phase, N: nematic phase, SmA: smectic A phase, Iso: isotropic phase, G: glass state).

| Entry                           | Phase Transition Behavior  |   |
|---------------------------------|--|---|
|                                 | Heating <sup>[a]</sup>   | Cooling <sup>[b]</sup>                            |
| <b>DPB[7]-C3</b> <sup>[c]</sup> | Cr 52.6 (11.8) N 160.4 (0.85) Iso                                | Iso 158.3 (0.86) N 4.8 (5.68) Cr                  |
| <b>M5</b>                       | Cr 37.9 (0.15) Cr2 <sup>[d]</sup> 66.4 (0.24) N 111.6 (0.33) Iso | Iso 109.8 (0.60) N                                |
| <b>M6</b>                       | Cr 77.4 (22.5) SmA 84.8 (0.49) N 109.3 (0.77) Iso                | Iso 107.5 (0.41) N 83.0 (0.49) SmA 29.5 (15.6) Cr |
| <b>P1</b>                       | G 60.6 N 176.3 (0.22) Iso  | Iso 173.4 (0.36) N 57.5 G                         |
| <b>P2</b>                       | N 205.0 (0.32) Iso   | Iso 202.5 (0.28) N                                |
| <b>P3</b>                       | G 25.6 SmA 150.3 (0.65) N 184.2 (0.32) Iso                       | Iso 181.8 (0.46) N 152.8 (1.28) SmA 23.2 G        |
| <b>P4</b>                       | SmA 193.8 (0.75) N 205.0 (0.19) Iso                              | Iso 202.0 (0.44) N 181.5 (1.18) SmA               |

<sup>[a]</sup> Third heating for **DPB[7]-C3** and **P1–P4**, and second heating for **M5** and **M6**. <sup>[b]</sup> Third cooling for **DPB[7]-C3** and **P1–P4** and second cooling for **M5** and **M6**. <sup>[c]</sup> Reported by Iwai et al. [54]. <sup>[d]</sup> A crystal–crystal phase transition was observed only for **M5**.

**M5** exhibited the N phase between 66.4 °C and 111.6 °C during the heating process, while **M6** exhibited the SmA phase between 77.4 °C and 84.8 °C and the N phase between 84.8 °C and 109.3 °C. POM images of the schlieren textures in the N phase for **M5** and **M6** are illustrated in Figures S11 and S12, and fan-shaped textures in the SmA phase of **M6** are also presented in Figure S12. The flexible chain length, excluding the terminal ester group, (in terms of carbon and oxygen atoms) is three or fewer for **M5** and four or more for **M6**. This trend is similar to our **DPB[7]** liquid crystals [58], where the SmA phase emerges when the flexible chain length exceeds three atoms.

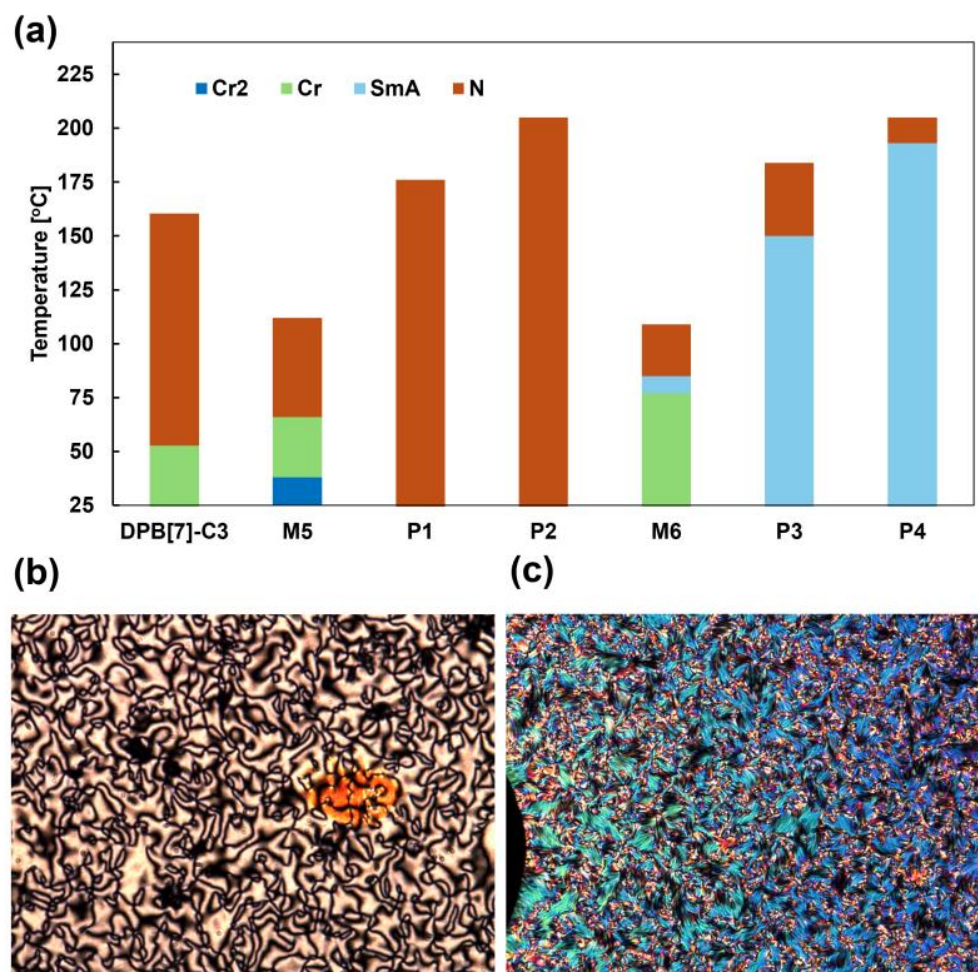


**Figure 1.** Summary of phase transition behavior. (a) Phase transition temperature and range diagram for DPB[7] monomers (DPB[7]-C3, M5, and M6) and DPB[7] polymers (P1–P4) observed by DSC measurement in second heating (for M5 and M6) and third heating (for DPB[7]-C3 and P1–P4) process. POM images of (b) schlieren texture for P2 at 193 °C and (c) fan-shape texture for P4 at 128 °C.

Next, we describe the phase transition behaviors of P1–P4. P1 and P2 exhibited N phases over the ranges of 25.0–176.3 °C and 25.0–205.0 °C, respectively, during the heating process. In these polymers, the N phase was successfully maintained at room temperature (25 °C), and schlieren textures were observed, as illustrated in Figure 1b. P3 displayed a smectic A (SmA) phase between 25.0 °C and 150.3 °C and an N phase from 150.3 °C to 184.2 °C, while P4 showed a SmA phase from 25.0 °C to 193.8 °C and an N phase from 193.8 °C to 205.0 °C. In the SmA phases of P3 and P4, fan-shaped textures were observed (Figure 1c). The glass transition temperature ( $T_g$ ) was observed at 60.6 °C for P1, and 25.6 °C for P3, while no  $T_g$  was detected for P2 and P4.

The clearing points of P1 and P2 were 64.7 °C and 93.4 °C higher than those of M5, respectively. Similarly, the clearing points of P3 and P4 were higher than those of M6 by 74.9 °C and 95.7 °C, respectively, and the N–SmA phase transition temperatures were higher by 65.5 °C and 109.0 °C. These results, indicating higher phase transition temperatures due to the polymer effect, are consistent with previously reported findings for SCLCPs. Notably, these liquid crystalline phases were maintained even after more than three months, as illustrated in Figures S13 and S14. The room temperature N phase observed in P1 and P2 offers significant advantages for optoelectronic applications operating at room temperature. Finally, upon 25.0 °C, the LC temperature ranges ( $\Delta T_{LC}$ ) for P1–P4 were 151.3 °C, 180.0 °C,



159.2 °C, and 180.0 °C, respectively. These values were considerably larger than those of the model monomers **M5** and **M6** ( $\Delta T_{LC} = 45.2$  °C and 31.9 °C, respectively).

### 2.3. Structure Analysis of LC Phase

To investigate changes in the molecular arrangement of the LCs due to polymer effect, we performed wide-angle X-ray diffraction (WAXD) measurements for **P1–P4** and the corresponding monomers **M5** and **M6** (Figures S17–S34). The WAXD profiles are summarized in Figure 2, in which the magnetic field is in the vertical direction of the paper. In the N phase, the peak observed in the small-angle region of the WAXD profile ( $2\theta_{\text{small}}$ ) corresponded to the layer spacing ( $d_{LC}$ ) along the molecular long axis. Also, in the SmA phase, not only the first-order peak ( $2\theta_{\text{small}}$ ) but also second- or third-order peaks were observed for P3 and P4, while the peak in the wide-angle region ( $2\theta_{\text{wide}}$ ) corresponded to the average distance between mesogens ( $d_{\text{mesogen}}$ ) along the molecular short axis. The values of the small-angle and wide-angle peaks ( $2\theta_{\text{small}}$ ,  $2\theta_{\text{wide}}$ ), along with the corresponding  $d$ -spacing values (calculated using Bragg's law) and the molecular length/side-chain length ( $l$ ) (obtained from DFT calculations (Figures S35 and S36, and Tables S1 and S2)) are presented in Table 3.

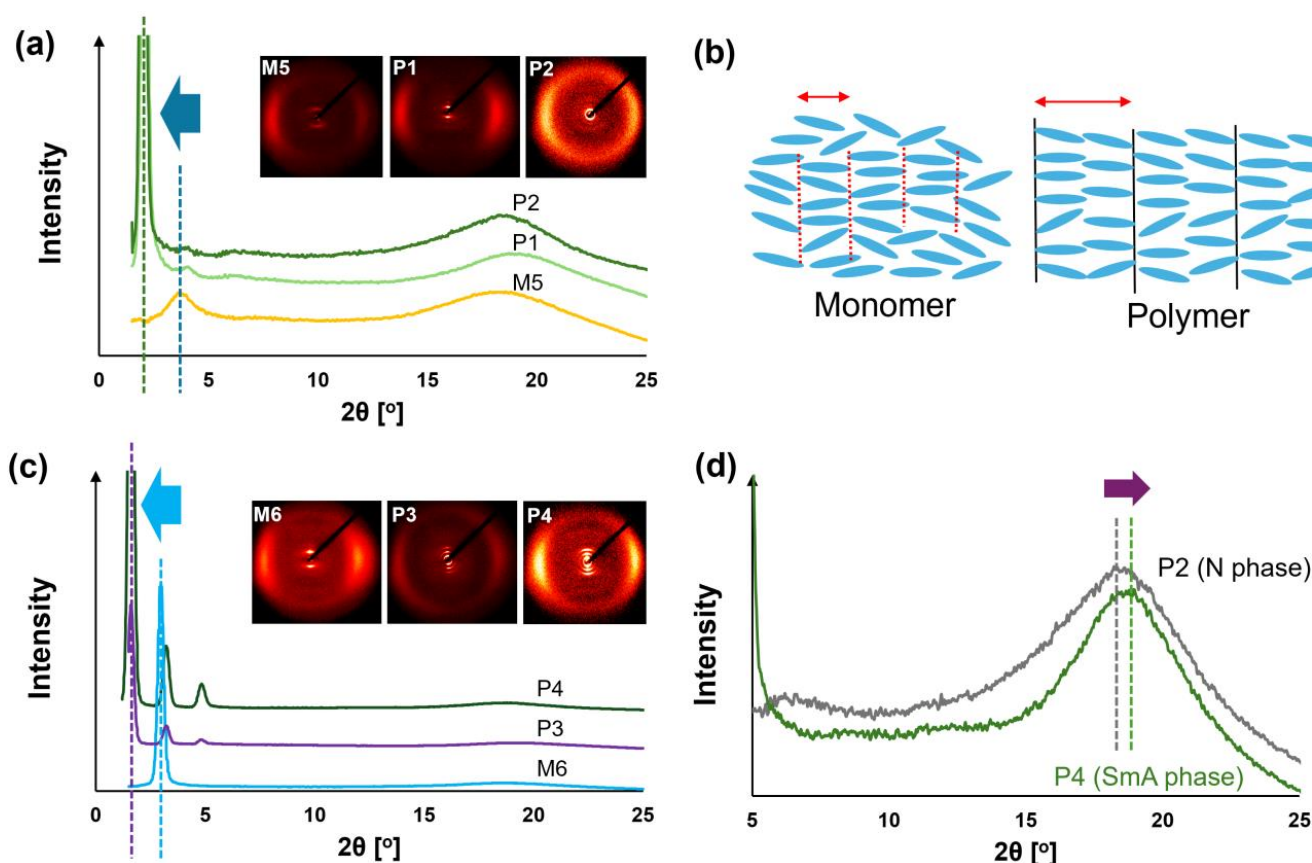


**Figure 2.** WAXD intensity profiles and expected structure in LC phase. (a) WAXD intensity profile in nematic (N) phase for **M5** (80 °C), **P1** (40 °C), and **P2** (30 °C). The  $2\theta_{\text{small}}$  values are shifted to small angle region due to the polymer effect. (b) Schematic illustration of molecular packing in N phase with cybotactic cluster for monomer (monolayer) and polymer (double-layer). (c) WAXD intensity profile in smectic A phase for **M6** (80 °C), **P3** (30 °C), and **P4** (30 °C). The  $2\theta_{\text{small}}$  values are shifted to small angle region due to the polymer effect. (d) WAXD intensity profile for **P2** and **P4** in wide-angle region recorded at 30 °C. The  $2\theta_{\text{wide}}$  value for SmA phase is slightly larger than that for N phase.

**Table 3.** The  $2\theta$  peak angle in small-angle region ( $2\theta_{\text{small}}$  [°]) and wide-angle region ( $2\theta_{\text{wide}}$  [°]) obtained from WAXD profile, their  $2\theta$   $d$ -spacing values ( $d_{\text{LC}}$  and  $d_{\text{mesogen}}$  [Å]), calculated molecular length ( $l$  [Å]), and the value of  $d_{\text{LC}}/l$ .

| Entry     | $2\theta_{\text{small}}$ [°] | $d_{\text{LC}}$ [a] [Å] | $l$ [b] [Å] | $d_{\text{LC}}/l$ [-] | $2\theta_{\text{wide}}$ [°] | $d_{\text{mesogen}}$ [Å] |
|-----------|------------------------------|-------------------------|-------------|-----------------------|-----------------------------|--------------------------|
| <b>M5</b> | 3.60 [c]                     | 24.6                    | 24.2        | 1.0                   | 18.5 [c]                    | 4.78                     |
| <b>P1</b> | 2.09                         | 42.4                    | 22.4        | 1.9                   | 18.9 [d]                    | 4.71                     |
| <b>P2</b> | 2.01 [e]                     | 44.0                    | 22.4        | 2.0                   | 18.3 [e]                    | 4.85                     |
| <b>M6</b> | 2.97 [c]                     | 29.8                    | 30.2        | 1.0                   | 18.5 [c]                    | 4.78                     |
| <b>P3</b> | 1.61 [e]                     | 55.1                    | 28.9        | 1.9                   | 19.3 [e]                    | 4.60                     |
| <b>P4</b> | 1.61 [e]                     | 55.1                    | 28.9        | 1.9                   | 18.9 [e]                    | 4.69                     |

[a] Layer spacing of LC phase (nematic phase for **M5**, **P1**, **P2**, and smectic A phase for **M6**, **P3**, **P4**) calculated from  $2\theta_{\text{small}}$  [°] value. [b] Whole molecular length (or length of side-chain for polymers) when alkyl chains are assumed to be fully extended in all-*trans* (calculated using DFT calculation at the B3LYP/6-31G(d) level of theory). [c] Measured at 80 °C. [d] Measured at 40 °C. [e] Measured at 30 °C.

In the N phase of **M5** (at 80 °C), **P1** (at 40 °C), and **P2** (at 30 °C), broad scattering peaks in the wide-angle region and sharp peaks in the small-angle region were observed (Figure 2a). In the N phase, there was no long-range positional order, and typically, only broad scattering in the wide-angle region was detected in WAXD measurements. Therefore, the observed small-angle peaks suggest the formation of smectic-like micro aggregates, specifically cybotactic clusters. The azimuthal profiles of diffraction in the small-angle region for **M5**, **P1**, and **P2** (Figures S19, S25 and S28) demonstrated that the scattering in the small-angle region was orthogonal to that in the wide-angle region. These results indicate that the cybotactic clusters [61–63] are SmA-type, with no uniform tilt in the domain. Notably, the ratio of the small-angle peak intensity to the wide-angle peak intensity was more than 10 times greater in **P1** and **P2** than in **M5**, suggesting that cybotactic clusters form more readily in **P1** and **P2** than in **M5**.

The  $2\theta_{\text{small}}$  values for **M5**, **P1**, and **P2** were 3.60°, 2.09°, and 2.01°, respectively, corresponding to  $d_{\text{LC}}$  values of 24.6 Å, 42.4 Å, and 44.0 Å, respectively. DFT calculations revealed that the molecular lengths ( $l$ ) for **M5**, **P1**, and **P3** were 24.2 Å, 22.4 Å, and 22.4 Å, respectively, when the flexible chains were in the all-*trans* configuration and fully extended. Consequently, the  $d_{\text{LC}}/l$  ratios for **M5**, **P1**, and **P3** were calculated to be 1.0, 1.9, and 2.0, respectively. This indicates that the cybotactic clusters in the N phase of **M5** form a monolayer structure, while those in **P1** and **P3** form a double-layer structure (Figure 2b).

In the SmA phase of **M6** (80 °C), **P3** (30 °C), and **P4** (30 °C), broad scattering peaks were observed in the wide-angle region, while sharp peaks appeared in the small-angle region. The azimuthal profiles of diffraction in the small-angle region for **M6**, **P3**, and **P4** (Figures S22, S31, and S34) showed that the scattering in the small-angle region was orthogonal to that in the wide-angle region, a characteristic of the SmA phase. The  $2\theta_{\text{small}}$  values for **M6**, **P3**, and **P4** were 2.97°, 1.61°, and 1.61°, respectively, corresponding to  $d_{\text{LC}}$  values of 29.8 Å, 55.1 Å, and 55.1 Å. DFT calculations revealed  $l = 30.2$  Å, 28.9 Å, and 28.9 Å for **M6**, **P3**, and **P4**, respectively, from which the  $d_{\text{LC}}/l$  ratios were determined to be 1.0, 1.9, and 1.9. This suggests that **M6** has a monolayer structure in the SmA phase, while **P3** and **P4** exhibit double-layer structures (Figure 2b).

In summary, **M5** and **M6** exhibit monolayer structures in the LC phase, while **P1–P4** form double-layer structures. The formation of a double-layer structure is commonly reported in SCLCPs [64,65]. The  $2\theta_{\text{wide}}$  values observed in the N phase of **M5**, **P1**, and **P2** were 18.5°, 18.9°, and 19.3°, respectively, while those observed in the SmA phase of **M6**, **P3**, and **P4** were 18.5°, 18.9°, and 19.3°, respectively. Consequently,  $d_{\text{mesogen}}$  values for **M5**, **P1**, **P2**, **M6**, **P3**, and **P4** were calculated to be 4.78 Å, 4.71 Å, 4.85 Å, 4.78 Å, 4.60 Å, and 4.69 Å, respectively. Although there was no difference between the  $d_{\text{mesogen}}$  values of **M5** and **M6**, the values of **P3** and **P4** were 0.02–0.25 Å smaller than those of **P1** and **P2**.

### 2.4. Birefringence Properties

To evaluate the optical properties of **P1–P4**, temperature-variable birefringence ( $\Delta n$ ) measurements were performed following our previously reported method [66–70]. For comparison with the corresponding polymers,  $\Delta n$  measurements were also conducted for **M5** and **M6** because of the lack of heat stability of **M1–M4**. First, the nematic liquid crystals (NLCs) were filled into homogeneously aligned polyimide cells. When preparing LC cells for **P1–P4**, the acrylic polymers **P1** and **P3** could be filled into the polyimide cells via capillary force; however, the methacrylic polymers **P2** and **P4** could not be filled due to their high viscosity, likely caused by differences in molecular weight. To confirm uniaxial orientation, POM observations were carried out. The prepared LC cells appeared dark when the polarizer was aligned with the rubbing direction and brightest when at  $45^\circ$  to the rubbing direction (Figure S37). These results confirm that the nematic director was aligned with the rubbing direction.

Next, we employed a micro-spectroscopic method, observing the transmitted light through the LC cell as a function of wavelength ( $\lambda$ ) under cross-polarized conditions. The nematic director was set at  $45^\circ$  to the polarizer. A typical transmission light plot is shown in Figure S38 (dot). The transmitted light intensity ( $I$ ) was fitted using the following Equation (1) and Cauchy's Equation (2) to determine the coefficients  $a$ ,  $b$ , and  $c$ , where  $A$  is a constant.

$$\frac{I}{I_0} = A \sin^2 \left( \frac{\pi \Delta n d}{\lambda} \right) \sin^2 \theta \quad (1)$$

$$\Delta n = a + \frac{b}{\lambda^2} + \frac{c}{\lambda^4} \quad (2)$$

The theoretical curve obtained from Equation (2) fitted well to the transmitted light plot (Figure S38 (solid line)). From this fitting, we obtained the  $\Delta n$  data presented in Figure 3. Figure 3a illustrates the wavelength dependence of  $\Delta n$  at  $T/T_i = 0.9$  ( $T_i$ : isotropic temperature), while Figure 3b shows  $\Delta n$  plotted against temperature for **M5**, **M6**, **P1**, and **P3** at 550 nm. As shown in Figure 3a, the  $\Delta n$  values of **P1** and **P3** were higher than those of **M5** and **M6**, indicating that  $\Delta n$  increased as a result of polymerization. Additionally, **P1** and **P3** exhibited  $\Delta n$  values of 0.24 and 0.20 at room temperature ( $25^\circ\text{C}$ ), respectively.

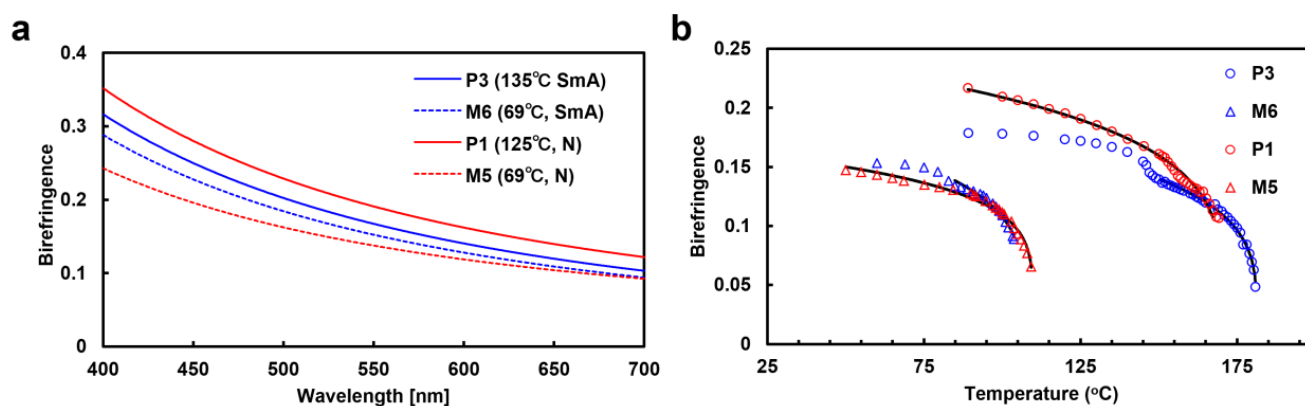


**Figure 3.** Birefringence is dependent on (a) wavelength and (b) temperature for **M5**, **M6**, **P1**, and **P3**. (a) Measured at the same reduced temperature ( $T/T_i = 0.9$ ) in each LC phase. (b) Plotted against temperature at 550 nm and fitted by Equations (3) and (4). For **M6** and **P3**, the fitting was performed within the nematic phase.

As illustrated in Figure 3b,  $\Delta n$  decreased with increasing temperature. The relationship between  $\Delta n$  and temperature can be explained by the temperature dependence of the order parameter ( $S$ ) of the nematic director, which is described by Haller's approximation:

$$\Delta n = \Delta n_0 S \quad (3)$$



$$S = \left(1 - \frac{T}{T_i}\right)^\beta \quad (4)$$

where  $\Delta n_0$  is the extrapolated value for the perfectly oriented birefringence ( $S = 1$ ) of the N LC,  $T_i$  is the clearing point, and  $\beta$  is a material constant characteristic of the NLC. The theoretical curve obtained from Equation (4) fitted well to the plot of  $\Delta n$  for each compound (Figure 3), and the values of  $\beta$  and  $\Delta n_0$  were determined. Additionally, the order parameter  $S$  was calculated using Equation (3) from the measured  $\Delta n$  values and the corresponding  $\Delta n_0$  values.

The values of  $S$  at 90 °C were calculated, as this was the temperature at which **M5**, **M6**, **P1**, and **P3** could be measured, and are shown in Table 4 along with the corresponding values of  $\beta$  and  $\Delta n_0$ . The  $\Delta n_0$  values for **M5**, **M6**, **P1**, and **P3** were 0.21, 0.26, 0.31, and 0.26, respectively, and the  $\beta$  values were 0.18, 0.23, 0.22, and 0.23, respectively. The  $S$  values at 90 °C were 0.60, 0.50, 0.69, and 0.69, respectively. Comparison of these values indicates an improvement in  $S$  due to the polymer effect [21].

**Table 4.** Determined values of  $\Delta n_0$  and  $\beta$  by Haller's approximation and estimated birefringence ( $\Delta n$ ) and order parameter ( $S$ ) at 90 °C.

| Entry     | $\Delta n_0$ | $\beta$ | $\Delta n$ (90 °C) | $S$ (90 °C) |
|-----------|--------------|---------|--------------------|-------------|
| <b>M5</b> | 0.21         | 0.18    | 0.12               | 0.60        |
| <b>M6</b> | 0.26         | 0.23    | 0.13 [a]           | 0.50 [b]    |
| <b>P1</b> | 0.31         | 0.22    | 0.22               | 0.69        |
| <b>P3</b> | 0.26         | 0.23    | 0.18 [a]           | 0.69 [b]    |

[a] Value in smectic A phase. [b] calculated using  $\Delta n$  (90 °C) value in smectic A phase.

Furthermore, a comprehensive evaluation of the  $S$  values, combined with the results from DSC and WAXD measurements, led to the conclusion that the significant increase in the higher phase transition temperatures (SmA–N and N–isotropic transitions) of **P1–P4** might be attributed to the enhancement of  $S$ , which resulted from the formation of a double-layer structure in the liquid crystalline phase.

### 2.5. Fluorescence Properties

To investigate the fluorescence properties of **M1–M4** and **P1–P4**, absorption spectra, fluorescence spectra, and fluorescence quantum yields ( $\Phi_{fl}$ ) were measured in a dilute THF solution and in the solid state. Additionally, the fluorescence spectra of cast films of **P1–P4** were measured. The obtained values for maximum absorption wavelength ( $\lambda_{abs}$ ), maximum fluorescence wavelength ( $\lambda_{fl}$ ), and  $\Phi_{fl}$  for **M1–M4** and **P1–P4** are summarized in Table 5.

The  $\lambda_{abs}$  values for all the monomers (**M1–M4**) in THF were 316 nm. The  $\Phi_{fl}$  values for **M1–M4** in THF solution were 0.02, while in the solid state, they were 0.43, 0.58, 0.61, and 0.48, respectively. This indicates that **M1–M4** exhibited aggregation-induced emission (AIE) properties. The AIE properties were further confirmed by aggregation experiments on **M2** and **P2** (Figure 4). The  $\lambda_{fl}$  values for **M1–M4** in the THF solution were approximately 400 nm, while in the solid state (polycrystalline state), they were 417, 407, 413, and 408 nm, respectively. These results suggest that the fluorescence in the solid state may be derived from aggregates rather than isolated monomers. This behavior was similar to that of our previously reported AIEgen, bridged stilbene [55].

The  $\lambda_{abs}$  value for **P1–P4** in THF was 316 nm. The  $\Phi_{fl}$  value for **P1–P4** in the THF solution was approximately 0.03, while in the solid state, the values were 0.14, 0.15, 0.35, and 0.18, respectively. **P1–P4** exhibited the same AIE properties as the monomers, and aggregation experiments with **P2** and **P4** yielded similar results to those of the monomers (Table S3). Similar redshifts in the  $\lambda_{fl}$  values for **P1–P4** in both the THF solution and the solid state were observed, mirroring the behavior of the monomers. These findings revealed that the luminescence properties of the bulk polymers and monomers were nearly

identical. Interestingly, the  $\lambda_{fl}$  values for **P1–P4** in the polymer films were 442, 456, 469, and 473 nm, respectively, redshifted by more than 27 nm compared with those in the solid state (polycrystalline state) (Figure 5). The relationship between the  $\lambda_{fl}$  of the films and the liquid crystalline phase at room temperature was also investigated. The  $\lambda_{fl}$  values for **P1** and **P2** (which exhibited the N phase) were around 450 nm, while those for **P3** and **P4** (which exhibited the SmA phase) were around 470 nm. These results suggest that the  $\lambda_{fl}$  in the films may vary depending on the liquid crystalline phase, with a relatively shorter wavelength shift in the N phase and a longer wavelength shift in the SmA phase. This indicates that the molecular orientation and interactions in different LC phases may affect the fluorescence properties.

**Table 5.** Spectroscopic properties for **M1–M4** and **P1–P4** in THF solution, solid state, and film.

| Entry     | $\lambda_{abs}$ [nm] |      | $\Phi_f$ [-] |     | $\lambda_{fl}$ [nm] |      |
|-----------|----------------------|------|--------------|-----|---------------------|------|
|           | THF                  | THF  | Solid [a]    | THF | Solid [a]           | Film |
| <b>M1</b> | 316                  | 0.02 | 0.43         | 399 | 417                 | -    |
| <b>M2</b> | 316                  | 0.02 | 0.58         | 399 | 407                 | -    |
| <b>M3</b> | 316                  | 0.02 | 0.61         | 401 | 413                 | -    |
| <b>M4</b> | 316                  | 0.02 | 0.48         | 400 | 408                 | -    |
| <b>P1</b> | 316                  | 0.03 | 0.14         | 407 | 415                 | 442  |
| <b>P2</b> | 316                  | 0.02 | 0.16         | 399 | 413                 | 456  |
| <b>P3</b> | 316                  | 0.03 | 0.35         | 400 | 413                 | 469  |
| <b>P4</b> | 316                  | 0.03 | 0.18         | 407 | 413                 | 473  |

[a] Polycrystalline solid.

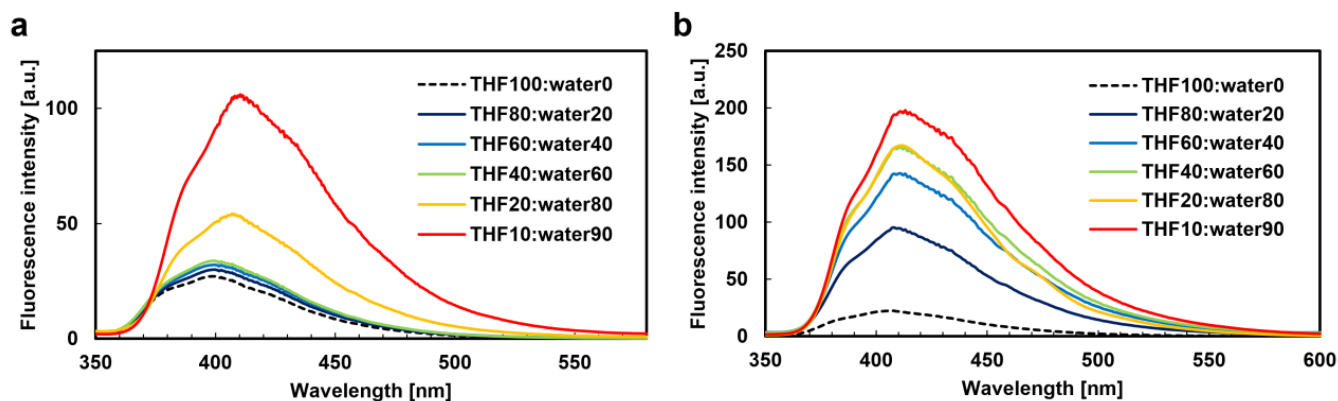


**Figure 4.** Aggregation experiments. Fluorescence spectra of (a) **M2** and (b) **P2** in THF/water mixtures with different water contents (vol %) excited at each  $\lambda_{abs}$ ; the concentration is  $10^{-5}$  M.

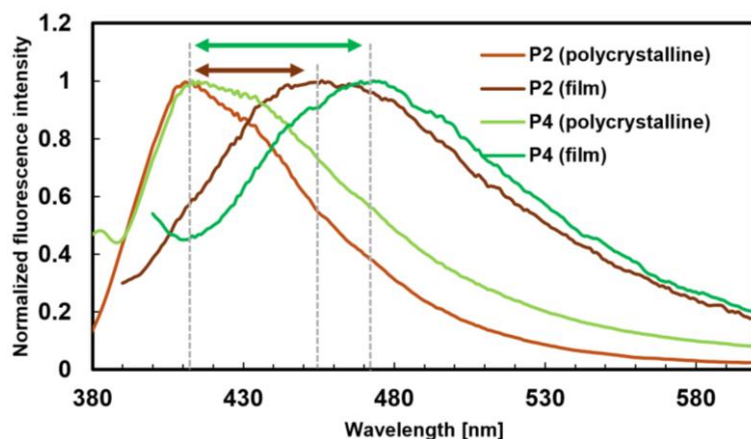


**Figure 5.** Fluorescence spectra of **P2** and **P4** excited at 370 nm (polycrystalline) and at 380 nm (film).

### 3. Experimental

#### 3.1. Materials

Unless otherwise noted, all solvents and chemicals were commercially available and used without further purification. Column chromatography was performed on silica gel (Silica Gel 60N, 63–210  $\mu\text{m}$ , Kanto chemical Co., Inc., Tokyo, Japan). [Hydroxy(tosyloxy)iodo]benzene, tetrakis(triphenylphosphine)palladium (0) ( $\text{Pd}(\text{PPh}_3)_4$ ), [1,1-bis(diphenylphosphino)ferrocene]palladium (0) ( $\text{Pd}(\text{dppf})\text{Cl}_2 \cdot \text{CH}_2\text{Cl}_2$ ), and 6-bromo-1-tetralone were purchased from TCI (Tokyo, Japan).

#### 3.2. Instruments

$^1\text{H}$ -NMR and  $^{13}\text{C}$ -NMR spectra were recorded on BRUKER 500 (Yokohama, Japan) (500 MHz) and JEOL 400 (Tokyo, Japan) (100 MHz) spectrometers, respectively, for  $\text{CDCl}_3$  solution using tetramethylsilane (TMS) as an internal standard.  $^1\text{H}$ -NMR spectra were reported as follows: chemical shift ( $\delta$  ppm), multiplicity (s = singlet, d = doublet, t = triplet, q = quartet, m = multiplet), integration, and coupling constants in units of Hz.  $^{13}\text{C}$ -NMR spectra were reported as chemical shifts in ppm. The FT-IR spectra were recorded on a JASCO FT-IR 4600 spectrometer (Tokyo, Japan). High-resolution EI mass spectra (HRMS) were recorded on a double-focusing mass spectrometer JEOL JMS-700, measured at the Tokyo Institute of Technology Open Facility Center. This center is independent of our laboratory to ensure fairness. Size exclusion chromatography (SEC) was performed using a JASCO system (PU-2080, CL-NETII/ADC, CO-2060, UV-2075, RI-2031, Tokyo, Japan) equipped with TSK gel columns (TOSOH G3000H xl, Tokyo, Japan) with THF as the eluent at the following rate of  $0.85 \text{ mL min}^{-1}$  at  $40 \text{ }^\circ\text{C}$  after calibration with polystyrene standards. Polarized optical microscopy (POM) was performed using a Leica DM2500P microscopy (Wetzlar, Germany) with a Mettler FP90 hot stage (Greifensee, Switzerland). Differential scanning calorimetry (DSC) was performed using PerkinElmer DSC 8500 equipment (Waltham, MA, USA) at a scanning rate of  $10 \text{ }^\circ\text{C min}^{-1}$  under a flow of dry nitrogen. Thermo-gravimetric analysis (TGA) was performed using a Rigaku Thermo Plus EVO2 series TG-DTA 8122 (Tokyo, Japan) at a heating rate of  $20 \text{ }^\circ\text{C min}^{-1}$  under a flow of dry nitrogen. The initial mass of the samples was 3–6 mg. X-ray investigations were carried out with samples kept in glass capillary tubes (1.0 mm diameter) for oriented patterns under a magnetic field. Wide-angle X-ray diffraction (WAXD) patterns were obtained using a Bruker D8 DISCOVER (Billerica, MA, USA) equipped with a Vantec-500 detector and Cu  $\text{K}\alpha$  radiation. UV-Vis spectra were recorded on a JASCO V-670 UV-vis spectrophotometer (Tokyo, Japan) and fluorescence spectra were recorded on a JASCO FP-6500 spectrofluorometer (Tokyo, Japan). Absolute quantum yields were measured by Hamamatsu Photonics Quantaurus QY apparatus (Hamamatsu City, Japan). All sample solutions were de-aerated by bubbling with argon for 15 min prior to the quantum yield measurement.

#### 3.3. Birefringence

Measurement of birefringence was performed in uniaxially aligned LC cells containing indium tin oxide (ITO) purchased from EHC. The cell gap ( $d$ ) of 3–5  $\mu\text{m}$  was determined by the interferometric method [66–70].

#### 3.4. Theoretical Calculations

Theoretical calculations were carried out on the Gaussian 16 program [71]. Geometry optimizations were carried out using DFT methods at the B3LYP with the 6-31G(d) basis. Whether the optimized geometry was at the stationary point without any imaginary frequency was checked by the frequency calculation performed at the optimized geometries using their level of theory.

### 3.5. Synthesis

#### 6-(4-ethylphenyl)-3,4-dihydronaphthalen-1(2H)-one (**6a**)

To a solution of 6-bromo-1-tetralone (**5**) (3.4 g, 15 mmol), 4-alkylphenylboronic acid (3.4 g, 22 mmol), potassium phosphate (9.5 g, 45 mmol) in solvent (30 mL/12 mL/6 mL; toluene/water/methanol), Pd(PPh<sub>3</sub>)<sub>4</sub> (0.55 g, 0.48 mmol) was added under argon atmosphere, and the mixture was refluxed (100 °C) for 3 hours. After the reaction, the mixture was cooled to room temperature, then extracted with dichloromethane. The organic layer was washed with water three times, dried over MgSO<sub>4</sub>, filtrated, and evaporated in vacuo. The residue was purified by column chromatography on silica gel (6/1 (v/v) hexane/ethyl acetate) to afford **6a** as a brown solid; yield 96%; <sup>1</sup>H-NMR (500 MHz, CDCl<sub>3</sub>) δ 8.09 (d, *J* = 8.2 Hz, Ar-*H*, 1H), 7.56–7.52 (m, Ar-*H*, 3H), 7.47–7.45 (m, Ar-*H*, 1H), 7.31–7.29 (m, Ar-*H*, 2H), 3.02 (t, *J* = 6.1 Hz, -CH<sub>2</sub>-, 2H), 2.73–2.67 (m, -CH<sub>2</sub>-, 4H), 2.20–2.15 (m, -CH<sub>2</sub>-, 2H), 1.28 (t, *J* = 7.6 Hz, -CH<sub>3</sub>, 3H) ppm (Figure S47).

#### 6-(4-ethylphenyl)-1-methylene-1,2,3,4-tetrahydronaphthalene (**7a**)

Methyltriphenylphosphonium bromide (7.1 g, 19 mmol) was dissolved in THF (40 mL) under argon atmosphere. The solution was cooled to 0 °C, and then potassium tert-butoxide (2.4 g, 21 mmol) was added. Following stirring for 10 minutes, **6a** (14.5 mmol) was added, warming to room temperature and stirring overnight. The reaction mixture was quenched by adding NH<sub>4</sub>Cl aq to the solution and extracted with ethyl acetate. The organic layer was washed with water three times, dried over MgSO<sub>4</sub>, filtrated, and evaporated in vacuo. The residue was purified by column chromatography on silica gel (4/1 (v/v) hexane/dichloromethane) to afford **7a** as a colorless solid; yield 90%; <sup>1</sup>H-NMR (500 MHz, CDCl<sub>3</sub>) δ 7.71 (d, *J* = 8.2 Hz, Ar-*H*, 1H), 7.51 (d, *J* = 8.2 Hz, Ar-*H*, 2H), 7.40–7.37 (m, Ar-*H*, 1H), 7.33–7.32 (m, Ar-*H*, 1H), 7.26 (d, *J* = 7.6 Hz, Ar-*H*, 2H), 5.51 (s, C=CH, 1H), 4.96 (s, C=CH, 1H), 2.90 (t, *J* = 6.3 Hz, -CH<sub>2</sub>-, 2H), 2.69 (q, *J* = 7.6 Hz, -CH<sub>2</sub>-, 2H), 2.57 (t, *J* = 6.1 Hz, -CH<sub>2</sub>-, 2H), 1.94–1.89 (m, -CH<sub>2</sub>-, 2H), 1.27 (t, *J* = 7.6 Hz, -CH<sub>3</sub>, 3H) ppm (Figure S49).

#### 2-(4-ethylphenyl)-5,7,8,9-tetrahydro-6H-benzo[7]annulen-6-one (**8a**)

To a solution of **7a** (13 mmol) in solvent (38 mL/2 mL; methanol/water), HTIB ([hydroxy(tosyloxy)iodo]benzene; 5.6 g, 14 mmol) was added under air, and stirred at room temperature for 20 min. After the reaction, the mixture was extracted with dichloromethane. The organic layer was washed with water three times, dried over MgSO<sub>4</sub>, filtrated, and evaporated in vacuo. The residue was purified by column chromatography on silica gel (6/1 (v/v) hexane/ethyl acetate) to afford **8a** as a colorless solid; yield 92%; <sup>1</sup>H-NMR (500 MHz, CDCl<sub>3</sub>) δ 7.51 (d, *J* = 8.2 Hz, Ar-*H*, 2H), 7.41–7.38 (m, Ar-*H*, 2H), 7.27 (d, *J* = 8.2 Hz, Ar-*H*, 2H), 7.21 (d, *J* = 7.6 Hz, Ar-*H*, 1H), 3.76 (s, -CH<sub>2</sub>-, 2H), 3.01 (t, *J* = 6.4 Hz, -CH<sub>2</sub>-, 2H), 2.69 (q, *J* = 7.6 Hz, -CH<sub>2</sub>-, 2H), 2.60 (t, *J* = 7.0 Hz, -CH<sub>2</sub>-, 2H), 2.06–2.01 (m, -CH<sub>2</sub>-, 2H), 1.28 (t, *J* = 7.6 Hz, -CH<sub>3</sub>, 3H) ppm (Figure S51).

#### 3-(4-ethylphenyl)-6,7-dihydro-5H-benzo[7]annulen-8-yl trifluoromethanesulfonate (**9a**)

The mixture of **8a** (12 mmol) and THF (30 mL) was cooled to –20 °C, and then tert-butoxide (2.4 g, 21 mmol) was added. The mixture was stirred at 0 °C for 1 h, and then cooled to –20 °C, then N-phenylbis(trifluoromethanesulfonimide) (5.3 g, 15 mmol) was added, and stirred at –20 °C for a further 1 h, and then warmed to 0 °C, and stirred for 4 h. After that, the reaction was quenched by the dropwise addition of water (20 mL), and organic products were extracted with ethyl acetate. The organic layer was washed with water three times, dried over MgSO<sub>4</sub>, filtrated, and evaporated in vacuo. The residue was purified by column chromatography on silica gel (6/1 (v/v) hexane/ethyl acetate) to afford **9a** as a slight yellow solid; yield 98%; <sup>1</sup>H-NMR (500 MHz, CDCl<sub>3</sub>) δ 7.51 (d, *J* = 7.9 Hz, Ar-*H*, 2H), 7.43–7.40 (m, Ar-*H*, 1H), 7.34–7.33 (m, Ar-*H*, 1H), 7.27 (d, *J* = 8.2 Hz, Ar-*H*, 2H), 7.22 (d, *J* = 7.9 Hz, Ar-*H*, 1H), 6.62 (s, Ar-CH-, 1H), 2.95 (t, *J* = 5.2 Hz, -CH<sub>2</sub>-, 2H), 2.81 (t, *J* = 6.4 Hz, -CH<sub>2</sub>-, 2H), 2.70 (q, *J* = 7.6 Hz, -CH<sub>2</sub>-, 2H), 2.06–2.01 (m, -CH<sub>2</sub>-, 2H), 1.28 (t, *J* = 7.6 Hz, -CH<sub>3</sub>, 3H) ppm (Figure S53).

*tert*-butyl(2-(4-(3-(4-ethylphenyl)-6,7-dihydro-5*H*-benzo[7]annulen-8-yl)phenoxy)ethoxy)-dimethylsilane (**10a**)

To a solution of **9** (8 mmol), **4a** (16 mmol),  $K_3PO_4 \cdot nH_2O$  (2.4 g, 16 mmol) in THF (40 mL),  $Pd(PPh_3)_4$  (0.28 g, 0.24 mmol) was added under argon atmosphere, and stirred at 50 °C overnight. After the reaction, the mixture was cooled to room temperature, then extracted with dichloromethane. The organic layer was washed with water three times, dried over  $MgSO_4$ , filtrated, and evaporated in vacuo. The residue was purified by column chromatography on silica gel (4/1 (*v/v*) hexane/dichloromethane) to afford **10a** as a colorless solid; yield 54%;  $^1H$ -NMR (500 MHz,  $CDCl_3$ )  $\delta$  7.55 (d,  $J = 7.9$  Hz, Ar-*H*, 2H), 7.45–7.39 (m, Ar-*H*, 4H), 7.27–7.26 (m, 3H), 6.91 (d,  $J = 8.5$  Hz, Ar-*H*, 2H), 6.77 (s, Ar-*H*, 1H), 4.07 (t,  $J = 5.3$  Hz,  $-CH_2-$ , 2H), 3.99 (t,  $J = 5.0$  Hz,  $-CH_2-$ , 2H), 2.87 (t,  $J = 6.0$  Hz,  $-CH_2-$ , 2H), 2.72–2.66 (m,  $-CH_2-$ , 4H), 2.23 (t,  $J = 6.3$  Hz,  $-CH_2-$ , 2H), 1.28 (t,  $J = 7.6$  Hz,  $-CH_3$ , 3H), 0.92 (s,  $CH_3$ , 9H), 0.12 (s,  $-CH_3$ , 6H) ppm (Figure S55).

2-(4-(3-(4-ethylphenyl)-6,7-dihydro-5*H*-benzo[7]annulen-8-yl)phenoxy)ethan-1-ol (**11a**)

To a solution of **10a** (2.6 mmol) in THF (5.0 mL), 12M HCl aq (4.0 mL) was added, and stirred at room temperature for 10 min. After that, the reaction was quenched by the dropwise addition of  $NaHCO_3$  aq (20 mL), and organic products were extracted with dichloromethane. The organic layer was washed with water three times, dried over  $MgSO_4$ , filtrated, and evaporated in vacuo. Purification by recrystallization ( $CHCl_3$ /Hex) gave **11a** as a colorless solid; yield 87%;  $^1H$ -NMR (500 MHz,  $CDCl_3$ )  $\delta$  7.55 (d,  $J = 8.2$  Hz, Ar-*H*, 2H), 7.46 (d,  $J = 8.7$  Hz, Ar-*H*, 2H), 7.42 (dd,  $J = 7.8, 2.0$  Hz, Ar-*H*, 1H), 7.39 (s, Ar-*H*, 1H), 7.28–7.26 (m, 3H), 6.93 (d,  $J = 8.9$  Hz, Ar-*H*, 2H), 6.78 (s, Ar-*H*, 1H), 4.12 (t,  $J = 4.6$  Hz,  $-CH_2-$ , 2H), 4.00–3.97 (m,  $-CH_2-$ , 2H), 2.88 (t,  $J = 6.1$  Hz,  $-CH_2-$ , 2H), 2.72–2.66 (m,  $-CH_2-$ , 4H), 2.26–2.21 (m,  $-CH_2-$ , 2H), 1.28 (t,  $J = 7.5$  Hz,  $-CH_2-$ , 3H) ppm (Figure S57).

2-(4-(3-(4-ethylphenyl)-6,7-dihydro-5*H*-benzo[7]annulen-8-yl)phenoxy)ethyl acrylate (**M1**)

To a solution of compound **11a** (1.3 mmol) and triethylamine (0.27 mL, 2.0 mmol) in dichloromethane (5.0 mL) was added acyl chloride (1.7 mmol) and the mixture was stirred at room temperature for 1 h. After the reaction, the solvent was removed by evaporation, and the residue was filtered with hexane. The organic layer was washed with water three times, dried over  $MgSO_4$ , filtrated, and evaporated in vacuo. The residue was purified by column chromatography on silica gel (1/1 (*v/v*) hexane/ethyl acetate) to afford crude M1-M6. Purification by recrystallization (hexane/dichloromethane) gave pure **M1** as a colorless solid; yield: 53%;  $^1H$ -NMR (500 MHz,  $CDCl_3$ )  $\delta$  7.55 (d,  $J = 8.2$  Hz, Ar-*H*, 2H), 7.47–7.39 (m, Ar-*H*, 4H), 7.27–7.25 (m, 3H), 6.93 (d,  $J = 8.5$  Hz, Ar-*H*, 2H), 6.77 (s, Ar-*H*, 1H), 6.48–6.44 (m, =CH, 1H), 6.18 (dd,  $J = 17.4, 10.4$  Hz,  $-CH=$ , 1H), 5.87 (dd,  $J = 10.5, 1.4$  Hz, =CH, 1H), 4.53 (t,  $J = 4.7$  Hz,  $-CH_2-$ , 2H), 4.25 (t,  $J = 4.9$  Hz,  $-CH_2-$ , 2H), 2.88 (t,  $J = 6.1$  Hz,  $-CH_2-$ , 2H), 2.72–2.66 (m,  $-CH_2-$ , 4H), 2.23 (t,  $J = 6.1$  Hz,  $-CH_2-$ , 2H), 1.28 (t,  $J = 7.6$  Hz,  $-CH_3$ , 3H) ppm (Figure S59);  $^{13}C$ -NMR (100 MHz,  $CDCl_3$ )  $\delta$  166.2, 157.9, 143.4, 142.3, 141.6, 139.2, 138.4, 137.4, 136.4, 131.5, 131.1, 128.4, 128.2, 127.7, 127.5, 127.4, 127.0, 124.5, 114.5, 66.1, 63.0, 35.0, 33.1, 30.3, 28.6, 15.7 ppm (Figure S60). HRMS (EI) Calcd for  $C_{30}H_{30}O_3$ : 438.5664, Found 438.2195 (Figure S57).

Poly[2-(4-(3-(4-ethylphenyl)-6,7-dihydro-5*H*-benzo[7]annulen-8-yl)phenoxy)ethyl] acrylate (**P1**)

To a pressure-resistant tube, which contained **M1** (0.37 g, 0.83 mmol) and a portion of THF (3.0 mL), AIBN (azobis(isobutyronitrile), 9.0 mg, 6.5 wt%), was added, and the mixture was stirred at 60 °C for 24 h. The mixture was poured dropwise with an excess amount of methanol, and it was filtered. The solids were purified by column chromatography on Sephadex<sup>TM</sup> G100 (eluted with THF), and reprecipitated with methanol; colorless solid; yield 40.3%;  $^1H$ -NMR (500 MHz,  $CDCl_3$ )  $\delta$  7.50–7.05 (brm, Ar-*H*, 9H), 6.88–6.71 (brm, Ar-*H*, 3H), 4.26–4.10 (brm, 4H), 2.88–2.36 (brm, 6H), 2.17–2.13 (brm, 2H), 1.84 (br, 1H), 1.26 (br, 3H) ppm (Figure S71);  $^{13}C$ -NMR (100 MHz,  $CDCl_3$ )  $\delta$  174.7, 157.8, 143.3, 142.1, 141.6, 139.0,



138.3, 138.2, 137.2, 136.3, 135.9, 131.2, 128.3, 127.4, 127.3, 126.9, 125.6, 124.5, 114.5, 65.8, 62.9, 41.3, 41.2, 35.0, 34.3, 33.1, 31.6, 30.4, 30.1, 29.6, 28.6, 21.3, 15.7 ppm (Figure S72).

#### 4. Conclusions

We synthesized **P1–P4** as SCLCPs with varying flexible chain lengths by radical polymerization of acrylate monomers containing  $\pi$ -extended bridged stilbene mesogens. The resulting polymers exhibited liquid crystalline phases over a temperature range exceeding 150 °C. **P1** and **P2** exhibited a nematic phase at room temperature, which was maintained for more than three months. These stable nematic phases are highly advantageous for device applications operating at room temperature. WAXD measurements revealed that the polymers possessed a double-layer structure in the liquid crystalline phase. Additionally, the polymers demonstrated larger order parameter ( $S$ ) values compared with small molecules and exhibited higher birefringence. The polymers were also found to retain the AIE characteristics of the **DPB[7]** skeleton, with high quantum yields ( $\Phi_{fl} = 0.14–0.35$ ) in the solid state (polycrystalline). Furthermore, film formation resulted in a redshift of the maximum fluorescence wavelength ( $\lambda_{fl}$ ) by more than 27 nm, yielding  $\lambda_{fl}$  values in the range of 442–473 nm. The magnitude of the redshift may be related to the liquid crystalline phase exhibited at room temperature, though further investigation is required to clarify the details. These optically and luminescent-functionalized SCLCPs hold promise for applications in luminescent semiconductors and optoelectronic materials, including holograms [72–74] and polarized light-emitting devices [75–85].

**Supplementary Materials:** The following supporting information can be downloaded at <https://www.mdpi.com/article/10.3390/molecules29215220/s1>: Figures S1–S4: TGA curves; Figures S5–S10: DSC thermogram; Figures S11–S16: POM images; Figures S17–S34: 1D- or 2D-WAXD profiles; Figures S35 and S36: Optimized structure (DFT calculation); Figure S37: POM images of nematic phase in polyimide cell; Figure S38: Wavelength dependence of light transmittance; Figure S39: Absorption spectra; Figure S40: Fluorescence spectra; Figures S41–S78: NMR spectra; Figures S79–S84: FT-IR spectra; Figures S85–S88: HRMS spectra; Tables S1 and S2: Atomic coordination and absolute energy (DFT calculation); Table S3: Aggregation experiments.

**Author Contributions:** Conceptualization, G.-i.K. and R.I.; methodology, M.T.; Formal analysis, Y.S. (Yoshimichi Shimomura), Y.S. (Yuki Sawatari) and M.T.; investigation, Y.S. (Yuki Sawatari), Y.S. (Yoshimichi Shimomura) and T.T.; writing—original draft, G.-i.K., Y.S. (Yuki Sawatari) and T.T.; writing—review and editing, G.-i.K.; project administration, G.-i.K. All authors have read and agreed to the published version of the manuscript.

**Funding:** This project was supported in part by MEXT/JSPS KAKENHI grants 23H02036 (G.-i.K.), JST PRESTO (G.-i.K.), Toshiaki Ogasawara Memorial Foundation (G.-i.K.), Iketani Science and Technology Foundation, Murata Science and Education Foundation (G.-i.K.), and Science Tokyo SPRING Foundation (Y.S.).

**Institutional Review Board Statement:** Not applicable.

**Informed Consent Statement:** Not applicable.

**Data Availability Statement:** The original contributions presented in this study are included in this article/Supplementary Materials, further inquiries can be directed to the corresponding author.

**Acknowledgments:** We thank Masato Koizumi (Materials Analysis Division, Tokyo Institute of Technology) for the HRMS measurements. This division is independent of our laboratory to ensure fairness. Riki Iwai and Y. Shimomura thank JSPS Research Fellowships for Young Scientists.

**Conflicts of Interest:** The authors declare no conflicts of interest.

## References

1. Jackson, W.J., Jr. Liquid crystal polymers. XI. Liquid crystal aromatic polyesters: Early history and future trends. *Mol. Cryst. Liq. Cryst.* **1989**, *169*, 23. [[CrossRef](#)]
2. White, T.; Broer, D. Programmable and adaptive mechanics with liquid crystal polymer networks and elastomers. *Nat. Mater.* **2015**, *14*, 1087. [[CrossRef](#)] [[PubMed](#)]
3. Imrie, C.T.; Henderson, P.A. Liquid crystal dimers and higher oligomers: Between monomers and polymers. *Chem. Soc. Rev.* **2007**, *36*, 2096. [[CrossRef](#)] [[PubMed](#)]
4. Watanabe, J.; Hayashi, M.; Nakata, Y.; Niori, T.; Tokita, M. Smectic liquid crystals in main-chain polymers. *Prog. Polym. Sci.* **1997**, *22*, 1053. [[CrossRef](#)]
5. Watanabe, Y.; Kato, R.; Fukushima, K.; Kato, T. Degradable and nanosegregated elastomers with multiblock sequences of biobased aromatic mesogens and biofunctional aliphatic oligocarbonates. *Macromolecules* **2022**, *55*, 10285. [[CrossRef](#)]
6. Watanabe, J.; Hayashi, M. Thermotropic liquid crystals of polyesters having a mesogenic p,p'-biphenyl unit. 1. Smectic A mesophase properties of polyesters composed of p,p'-biphenyl and alkylene glycols. *Macromolecules* **1988**, *21*, 278. [[CrossRef](#)]
7. Watanabe, J.; Hayashi, M. Thermotropic liquid crystals of polyesters having a mesogenic p,p'-biphenyl unit. 2. X-ray study on smectic mesophase structures of BB-5 and BB-6. *Macromolecules* **1989**, *22*, 4083. [[CrossRef](#)]
8. Zhang, Y.; Wang, X.; Yang, W.; Yan, H.; Zhang, X.; Han, D.; He, Y.; Li, C.; Sun, L. Programmable Complex Shape Changing of Polysiloxane Main-Chain Liquid Crystalline Elastomers. *Molecules* **2023**, *28*, 4858. [[CrossRef](#)]
9. Shaya, J.; Ribierre, J.-C.; Correia, G.; Dappe, Y.J.; Mathevet, F.; Mager, L.; Heinrich, B.; Méry, S. Control of the Organization of 4,4'-bis(carbazole)-1,1'-biphenyl (CBP) Molecular Materials through Siloxane Functionalization. *Molecules* **2023**, *28*, 2038. [[CrossRef](#)]
10. Kim, J.G.; Lee, J.G.; Wie, J.J. Confinement-Induced Fabrication of Liquid Crystalline Polymeric Fibers. *Molecules* **2022**, *27*, 5639. [[CrossRef](#)]
11. Zhou, Z.; Li, W.; Qian, J.; Liu, W.; Wang, Y.; Zhang, X.; Guo, Q.; Yashchyn, Y.; Wang, Q.; Shi, Y.; et al. Flexible Liquid Crystal Polymer Technologies from Microwave to Terahertz Frequencies. *Molecules* **2022**, *27*, 1336. [[CrossRef](#)] [[PubMed](#)]
12. Xie, C.; Yang, S.; He, R.; Liu, J.; Chen, Y.; Guo, Y.; Guo, Z.; Qiu, T.; Tuo, X. Recent Advances in Self-Assembly and Application of Para-Aramids. *Molecules* **2022**, *27*, 4413. [[CrossRef](#)] [[PubMed](#)]
13. Shimomura, Y.; Kawamura, A.; Tokita, M.; Watanabe, J.; Konishi, G. Fluorinated Poly(pentylene 4,4'-biphenyl) with Low Isotropization Temperatures and Unique Phase Transition Behavior. *Macromolecules* **2023**, *56*, 5152. [[CrossRef](#)]
14. Kasai, H.; Hayakawa, Y.; Akiyama, H.; Ozaki, M.; Kato, T.; Kakimoto, M. New Fabrication Approach to Develop a High Birefringence Photo-Crosslinked Film Based on a Sulfur-Containing Liquid Crystalline Molecule with Large Temperature Dependence of Birefringence. *Mol. Cryst. Liq. Cryst.* **2018**, *671*, 28–35. [[CrossRef](#)]
15. McArdle, C.B. *Side Chain Liquid Crystal Polymers*; Springer: Dordrecht, The Netherlands; Loctite Ltd.: Dublin, Ireland, 1989.
16. Ikeda, T.; Tsutsumi, O. Optical Switching and Image Storage by Means of Azobenzene Liquid-Crystal Films. *Science* **1995**, *268*, 1873. [[CrossRef](#)]
17. Hisano, K.; Aizawa, M.; Ishizu, M.; Kurata, Y.; Nakano, W.; Akamatsu, N.; Christopher, J.; Shishido, A. Scanning wave photopolymerization enables dye-free alignment patterning of liquid crystals. *Sci. Adv.* **2017**, *3*, e1701610. [[CrossRef](#)]
18. Takahashi, K.; Taguchi, D.; Kajitani, T.; Fukushima, T.; Kubo, S.; Shishido, A. Synthesis and Characterization of Side-Chain Liquid-Crystalline Block Copolymers Containing Cyano-Terminated Phenyl Benzoate Moieties. *Molecules* **2023**, *28*, 7849. [[CrossRef](#)]
19. Shigeyama, T.; Matsumoto, K.; Hisano, K.; Tsutsumi, O. Tunable Reflection through Size Polydispersity of Chiral-Nematic Liquid Crystal Polymer Particles. *Molecules* **2023**, *28*, 7779. [[CrossRef](#)]
20. Arakawa, Y.; Nakajima, S.; Kang, S.; Konishi, G.; Watanabe, J. Synthesis and evaluation of high-birefringence polymethacrylate having a diphenyl-diacetylene LC moiety in the side chain. *J. Mater. Chem.* **2012**, *22*, 14346. [[CrossRef](#)]
21. Kang, S.; Nakajima, S.; Arakawa, Y.; Tokita, M.; Watanabe, J.; Konishi, G. Highly birefringent side-chain LC polymethacrylate with a dinaphthyl-acetylene mesogenic unit. *Polym. Chem.* **2014**, *5*, 2253. [[CrossRef](#)]
22. Ma, X.; Li, Q.; Song, C.; Zhang, H.; Zhi, Y.; He, X. The effect of different photoluminescent side-chain length on the phase behaviour of chiral liquid crystal polymer. *Liq. Cryst.* **2022**, *49*, 1498–1510. [[CrossRef](#)]
23. Castro, L.D.C.; Lub, J.; Oliveira, O.N., Jr.; Schenning, A.P.H.J. Mechanochromic Displays Based on Photoswitchable Cholesteric Liquid Crystal Elastomers. *Angew. Chem. Int. Ed.* **2024**, e202413559. [[CrossRef](#)]
24. Xiong, Y.; He, P. A review on electrocatalysis for alkaline oxygen evolution reaction (OER) by Fe-based catalysts. *J. Mater. Sci.* **2023**, *58*, 2041. [[CrossRef](#)]
25. Arakawa, Y.; Kuwahara, H.; Sakajiri, K.; Kang, S.; Tokita, M.; Konishi, G. Highly birefringent polymer films from the photocrosslinking polymerisation of bistolane-based methacrylate monomers. *Liq. Cryst.* **2015**, *42*, 1419. [[CrossRef](#)]
26. O'Neill, M.; Kelly, S.M. Ordered Materials for Organic Electronics and Photonics. *Adv. Mater.* **2010**, *23*, 566. [[CrossRef](#)]
27. Swager, T.M. Molecular Shape and Polar Order in Columnar Liquid Crystals. *Acc. Chem. Res.* **2022**, *55*, 3010. [[CrossRef](#)]
28. Hoeben, F.J.M.; Jonkheijm, P.; Meijer, E.W.; Schenning, A.P.H.J. About Supramolecular Assemblies of  $\pi$ -Conjugated Systems. *Chem. Rev.* **2005**, *105*, 1491. [[CrossRef](#)]

29. Sakurai, T.; Kato, K.; Shimizu, M. Side-Chain Labeling Strategy for Forming Self-Sorted Columnar Liquid Crystals from Binary Discotic Systems. *Crystals* **2023**, *13*, 1473. [[CrossRef](#)]
30. Demus, D.; Goodby, J.; Gray, G.W.; Spiess, H.W.; Vill, V. *Physical Properties of Liquid Crystals*; Wiley-VCH: Weinheim, Germany; New York, NY, USA; Chichester, UK; Brisbane, Australia; Singapore; Toronto, ON, Canada, 1999.
31. Heilmeyer, G.H.; Zannoni, L.A.; Barton, L.A. Guest-Host Interactions in Nematic Liquid Crystals. A New Electro-Optic Effect. *Appl. Phys. Lett.* **1968**, *13*, 91. [[CrossRef](#)]
32. Heilmeyer, G.H. Liquid crystal displays: An experiment in interdisciplinary research that worked. *IEEE Trans. Electron. Devices* **1976**, *23*, 780. [[CrossRef](#)]
33. O'Neill, M.; Kelly, S.M. Liquid crystals for charge transport, luminescence, and photonics. *Adv. Mater.* **2003**, *15*, 1135. [[CrossRef](#)]
34. Giménez, R.; Piñol, M.; Serrano, J.L. Luminescent liquid crystals derived from 9,10-bis(phenylethynyl)anthracene. *Chem. Mater.* **2004**, *16*, 1377. [[CrossRef](#)]
35. Fleischmann, E.K.; Zentel, R. Liquid-crystalline ordering as a concept in materials science: From semiconductors to stimuli-responsive devices. *Angew. Chem. Int. Ed.* **2013**, *52*, 8810. [[CrossRef](#)] [[PubMed](#)]
36. Iino, H.; Usui, T.; Hanna, J. Liquid crystals for organic thin-film transistors. *Nat. Commun.* **2015**, *6*, 6828. [[CrossRef](#)]
37. Padalkar, V.S.; Tsutsui, Y.; Sakurai, T.; Sakamaki, D.; Tohno, N.; Kato, K.; Takata, M.; Akutagawa, T.; Sakai, K.; Seki, S. Optical and structural properties of ESIPT inspired HBT-fluorene molecular aggregates and liquid crystals. *J. Phys. Chem. B.* **2017**, *121*, 10407. [[CrossRef](#)]
38. Zhang, W.; Sakurai, T.; Aotani, M.; Watanabe, G.; Yoshida, H.; Padalkar, V.S.; Tsutsui, Y.; Sakamaki, D.; Ozaki, M.; Seki, S. Highly fluorescent liquid crystals from excited-state intramolecular proton transfer molecules. *Adv. Opt. Mater.* **2019**, *7*, 1801349. [[CrossRef](#)]
39. Arakawa, Y.; Sasaki, S.; Igawa, K.; Tokita, M.; Konishi, G.; Tsuji, H. Birefringence and photoluminescence properties of diphenylacetylene-based liquid crystal dimers. *New J. Chem.* **2020**, *44*, 17531. [[CrossRef](#)]
40. Voskuhl, J.; Giese, M. Mesogens with aggregation-induced emission properties: Materials with a bright future. *Aggregate* **2022**, *3*, e124. [[CrossRef](#)]
41. Yamada, S.; Yoshida, K.; Uto, E.; Yoshida, K.; Sakurai, T.; Konno, T. Development of photoluminescent liquid-crystalline dimers bearing two fluorinated tolane-based luminous mesogens. *J. Mol. Liq.* **2023**, *363*, 119884. [[CrossRef](#)]
42. Yamada, S.; Konno, T. Development of donor- $\pi$ -acceptor-type fluorinated tolanes as compact condensed phase luminophores and applications in photoluminescent liquid-crystalline molecules. *Chem. Rec.* **2023**, *23*, e202300094. [[CrossRef](#)]
43. Wu, X.; Niu, X.; Zhu, S.; Tian, M.; Liu, W. A novel multi-stimuli responsive fluorescence liquid crystal material with aggregation-induced emission effect. *Liq. Cryst.* **2023**, *50*, 1035. [[CrossRef](#)]
44. Sawatari, Y.; Shimomura, Y.; Takeuchi, M.; Iwai, R.; Tanaka, T.; Tsurumaki, E.; Tokita, M.; Watanabe, J.; Konishi, G. Supramolecular liquid crystals from the dimer of L-shaped molecules with tertiary amide end groups. *Aggregate* **2024**, *5*, e507. [[CrossRef](#)]
45. Iida, Y.; Shimomura, Y.; Tokita, M.; Konishi, G. Push-pull biphenyl and tolane derivatives as novel luminescent liquid crystals: Synthesis and properties. *Liq. Cryst. Early View.* **2024**, 1–14. [[CrossRef](#)]
46. Pathak, S.K.; Pradhan, B.; Gupta, M.; Pal, S.K.; Sudhakar, A.A. Liquid-Crystalline Star-Shaped Supergelator Exhibiting Aggregation-Induced Blue Light Emission. *Langmuir* **2016**, *32*, 9301. [[CrossRef](#)]
47. Demus, D. One Century Liquid Crystal Chemistry: From Vorländer's Rods to Disks, Stars and Dendrites. *Mol. Cryst. Liq. Cryst.* **2006**, *364*, 25. [[CrossRef](#)]
48. Mei, J.; Leung, N.L.; Kwok, R.T.; Lam, J.W.; Tang, B.Z. Aggregation-Induced Emission: Together We Shine, United We Soar! *Chem. Rev.* **2015**, *115*, 11718. [[CrossRef](#)]
49. Sasaki, S.; Suzuki, S.; Sameera, W.M.C.; Igawa, K.; Morokuma, K.; Konishi, G. Highly Twisted N,N-Dialkylamines as a Design Strategy to Tune Simple Aromatic Hydrocarbons as Steric Environment-Sensitive Fluorophores. *J. Am. Chem. Soc.* **2016**, *138*, 8194. [[CrossRef](#)]
50. Suzuki, S.; Sasaki, S.; Sairi, A.S.; Iwai, R.; Tang, B.Z.; Konishi, G.I. Principles of Aggregation-Induced Emission: Design of Deactivation Pathways for Advanced AIEgens and Applications. *Angew. Chem. Int. Ed.* **2020**, *59*, 9856. [[CrossRef](#)]
51. Shen, Z.; Pan, Y.; Yan, D.; Wang, D.; Tang, B.Z. AIEgen-Based Nanomaterials for Bacterial Imaging and Antimicrobial Applications: Recent Advances and Perspectives. *Molecules* **2023**, *28*, 2863. [[CrossRef](#)]
52. Luo, W.; Tan, Y.; Gui, Y.; Yan, D.; Wang, D.; Tang, B.Z. Near-Infrared-Emissive AIE Bioconjugates: Recent Advances and Perspectives. *Molecules* **2022**, *27*, 3914. [[CrossRef](#)]
53. Zhou, L.; Zheng, L.L.; Gao, M.Y.; Xu, C.J.; Ge, Y.F.; Bai, T.X.; Wen, J.; Cheng, Y.H.; Zhu, M.F. Confinement fluorescence effect of an aggregation-induced emission luminogen in crystalline polymer. *Aggregate* **2023**, *4*, e338. [[CrossRef](#)]
54. Kumari, B.; Dahiwardkar, R.; Kanvah, S. White light emission from AIE-active luminescent organic materials. *Aggregate* **2022**, *3*, e191. [[CrossRef](#)]
55. Iwai, R.; Suzuki, S.; Sasaki, S.; Sairi, A.S.; Igawa, K.; Suenobu, T.; Morokuma, K.; Konishi, G. Bridged Stilbenes: AIEgens Designed via a Simple Strategy to Control the Non-radiative Decay Pathway. *Angew. Chem. Int. Ed.* **2020**, *59*, 10566. [[CrossRef](#)]
56. Shimomura, Y.; Konishi, G. Flexible Alkylene Bridges as a Tool to Engineer Crystal Distyrylbenzene Structures Enabling Highly Fluorescent Monomeric Emission. *Chem. Eur. J.* **2022**, *28*, e202201884. [[CrossRef](#)]

57. Shimomura, Y.; Konishi, G. Push-Pull Bridged Distyrylbenzene with Highly Bright Solid-State Red-Orange Aggregation-Induced Emission. *Chem. Eur. J.* **2023**, *29*, e20231191. [[CrossRef](#)]
58. Iwai, R.; Yoshida, H.; Arakawa, Y.; Sasaki, S.; Iida, Y.; Igawa, K.; Sakurai, T.; Suzuki, S.; Tokita, M.; Watanabe, J.; et al. Near-room-temperature  $\pi$ -conjugated nematic liquid crystals in molecules with a flexible seven-membered ring structure. *Aggregate* **2024**, *5*, e660. [[CrossRef](#)]
59. Miyaura, N.; Suzuki, A. Palladium-Catalyzed Cross-Coupling Reactions of Organoboron Compounds. *Chem. Rev.* **1995**, *95*, 245. [[CrossRef](#)]
60. Sen, A.; Yamada, Y.M. Latest Developments on Palladium- and Nickel-Catalyzed Cross-Couplings Using Aryl Chlorides: Suzuki–Miyaura and Buchwald–Hartwig Reactions. *Synthesis* **2024**, *56*. [[CrossRef](#)]
61. Arakawa, Y.; Sasaki, Y.; Haraguchi, N.; Itsuno, S.; Tsuji, H. Synthesis, phase transitions and birefringence of novel liquid crystalline 1,4-phenylene bis(4-alkylthio benzoates) and insights into the cybotactic nematic behaviour. *Liq. Cryst.* **2017**, *45*, 821. [[CrossRef](#)]
62. Shanker, G.; Prehm, M.; Nagaraj, M.; Vij, J.K.; Tschierske, C. Development of polar order in a bent-core liquid crystal with a new sequence of two orthogonal smectic and an adjacent nematic phase. *J. Mater. Chem.* **2011**, *21*, 18711. [[CrossRef](#)]
63. Mohamed, A.; Silvio, P.; Christoph, K.; Christoph, K.; Alexey, E.; Carsten, T. Cluster phases of 4-cyanoresorcinol derived hockey-stick liquid crystals. *J. Mater. Chem. C* **2017**, *5*, 8454. [[CrossRef](#)]
64. Yuan, Y.; Li, J.; He, L.; Liu, Y.; Zhang, H. Preparation and properties of side chain liquid crystalline polymers with aggregation-induced emission enhancement characteristics. *J. Mater. Chem. C* **2018**, *6*, 7119. [[CrossRef](#)]
65. Ni, B.; Liao, J.; Chen, S.; Zhang, H. Influence of alkoxy tail length on the phase behaviors of side-chain liquid crystalline polymers without the spacer. *RSC Adv.* **2015**, *5*, 9035. [[CrossRef](#)]
66. Arakawa, Y.; Nakajima, S.; Ishige, R.; Uchimura, M.; Kang, S.; Konishi, G.; Watanabe, J. Synthesis of diphenyl-diacetylene-based nematic liquid crystals and their high birefringence properties. *J. Mater. Chem.* **2012**, *22*, 8394. [[CrossRef](#)]
67. Kang, S.; Nakajima, S.; Arakawa, Y.; Konishi, G.; Watanabe, J. Large extraordinary refractive index in highly birefringent nematic liquid crystals of dinaphthyl-diacetylene-based materials. *J. Mater. Chem. C* **2013**, *1*, 4222. [[CrossRef](#)]
68. Arakawa, Y.; Kang, S.; Nakajima, S.; Sakajiri, K.; Cho, Y.; Kawachi, S.; Watanabe, J.; Konishi, G. Diphenyltriacetylenes: Novel nematic liquid crystal materials and analysis of their nematic phase-transition and birefringence behaviours. *J. Mater. Chem. C* **2013**, *1*, 8094. [[CrossRef](#)]
69. Arakawa, Y.; Kang, S.; Tsuji, H.; Watanabe, J.; Konishi, G. The design of liquid crystalline bistolane-based materials with extremely high birefringence. *RSC Adv.* **2016**, *6*, 92845. [[CrossRef](#)]
70. Arakawa, Y.; Kang, S.; Tsuji, H.; Watanabe, J.; Konishi, G. Development of novel bistolane-based liquid crystalline molecules with an alkylsulfanyl group for highly birefringent materials. *RSC Adv.* **2016**, *6*, 16568. [[CrossRef](#)]
71. Frisch, M.J.; Trucks, G.W.; Schlegel, H.B.; Scuseria, G.E.; Robb, M.A.; Cheeseman, J.R.; Scalmani, G.; Barone, V.; Petersson, G.A.; Nakatsuji, H.; et al. *Gaussian 16, Revision C.01*; Gaussian, Inc.: Wallingford, CT, USA, 2016.
72. Kim, J.; Li, Y.; Miskiewicz, M.N.; Oh, C.; Kudenov, M.W.; Escuti, M.J. Fabrication of ideal geometric-phase holograms with arbitrary wavefronts. *Optica* **2015**, *2*, 958. [[CrossRef](#)]
73. Pi, D.; Liu, J.; Wang, Y. Review of computer-generated hologram algorithms for color dynamic holographic three-dimensional display. *Light Sci. Appl.* **2022**, *11*, 231. [[CrossRef](#)]
74. Shishido, A. Rewritable holograms based on azobenzene-containing liquid-crystalline polymers. *Polym. J.* **2010**, *42*, 525. [[CrossRef](#)]
75. Kobashi, J.; Yoshida, H.; Ozaki, M. Polychromatic Optical Vortex Generation from Patterned Cholesteric Liquid Crystals. *Phys. Rev. Lett.* **2016**, *116*, 253903. [[CrossRef](#)] [[PubMed](#)]
76. Morita, F.; Kishida, Y.; Sato, Y.; Sugiyama, H.; Abekura, M.; Nogami, J.; Toriumi, N.; Nagashima, Y.; Kinoshita, T.; Fukuhara, G.; et al. Design and enantioselective synthesis of 3D  $\pi$ -extended carbohelicenes for circularly polarized luminescence. *Nat. Synth.* **2024**, *3*, 774. [[CrossRef](#)]
77. Hsieh, Y.-Y.; Shyue, J.-J.; Chao, Y.-C.; Wong, K.-T.; Bassani, D.M. Chiral Binaphthalene Building Blocks for Self-Assembled Nanoscale CPL Emitters. *Molecules* **2023**, *28*, 3382. [[CrossRef](#)] [[PubMed](#)]
78. Furoida, A.; Daitani, M.; Hisano, K.; Tsutsumi, O. Aggregation-Enhanced Room-Temperature Phosphorescence from Au(I) Complexes Bearing Mesogenic Biphenylethynyl Ligands. *Molecules* **2021**, *26*, 7255. [[CrossRef](#)] [[PubMed](#)]
79. Kato, K.; Iwano, R.; Tokuda, S.; Yasuzawa, K.; Gon, M.; Ohtani, S.; Furukawa, S.; Tanaka, K.; Ogoshi, T. Circularly polarized luminescence from a common alkoxy pillar [5]arene and its co-aggregates with  $\pi$ -conjugated rods. *Aggregate* **2024**, *5*, e482. [[CrossRef](#)]
80. Gong, Z.L.; Li, Z.Q.; Zhong, Y.W. Circularly polarized luminescence of coordination aggregates. *Aggregate* **2022**, *3*, e177. [[CrossRef](#)]
81. Yan, H.; He, Y.; Wang, D.; Han, T.; Tang, B.Z. Aggregation-induced emission polymer systems with circularly polarized luminescence. *Aggregate* **2023**, *4*, e331. [[CrossRef](#)]
82. Uchimura, M.; Watanabe, Y.; Araoka, F.; Watanabe, J.; Takezoe, H.; Konishi, G. Development of Laser Dyes to Realize Low Threshold in Dye-Doped Cholesteric Liquid Crystal Lasers. *Adv. Mater.* **2010**, *22*, 4473. [[CrossRef](#)]
83. Wan, S.-P.; Lu, H.-Y.; Li, M.; Chen, C.-F. Advances in circularly polarized luminescent materials based on axially chiral compounds. *J. Photochem. Photobiol. C* **2022**, *50*, 100500. [[CrossRef](#)]

84. Hasegawa, Y.; Kitagawa, Y. Luminescent lanthanide coordination polymers with transformative energy transfer processes for physical and chemical sensing applications. *J. Photochem. Photobiol. C* **2022**, *51*, 100485. [[CrossRef](#)]
85. Cho, S.; Takahashi, M.; Fukuda, J.; Yoshida, H.; Ozaki, M. Directed self-assembly of soft 3D photonic crystals for holograms with omnidirectional circular-polarization selectivity. *Commun. Mater.* **2021**, *2*, 39. [[CrossRef](#)]

**Disclaimer/Publisher's Note:** The statements, opinions and data contained in all publications are solely those of the individual author(s) and contributor(s) and not of MDPI and/or the editor(s). MDPI and/or the editor(s) disclaim responsibility for any injury to people or property resulting from any ideas, methods, instructions or products referred to in the content.